



Determination of the exchange anisotropy in perovskite antiferromagnets using powder inelastic neutron scattering

R. J. McQueeney

Department of Physics and Astronomy and Ames Laboratory, Iowa State University, Ames, Iowa 50011, USA

J.-Q. Yan and S. Chang*

Ames Laboratory, Iowa State University, Ames, Iowa 50011, USA

J. Ma

Department of Physics and Astronomy, Iowa State University, Ames, Iowa 50011, USA

(Received 1 July 2008; revised manuscript received 12 September 2008; published 17 November 2008)

A procedure is outlined for the determination of magnetic exchange constants in anisotropic perovskite antiferromagnets using powder inelastic neutron scattering. Spin-wave densities of states are measured using time-of-flight inelastic neutron scattering for LaMnO_3 (*A*-type antiferromagnet), LaVO_3 (*C* type), and LaFeO_3 (*G* type) and compared to Heisenberg model calculations. The anisotropy of in-plane (J_{ab}) and out-of-plane (J_c) exchange constants can be obtained from the data. The procedure quickly determines the magnetic exchange interactions without the need for single-crystal dispersion measurements and allows for rapid systematic studies of the evolution of magnetism in perovskite systems.

DOI: [10.1103/PhysRevB.78.184417](https://doi.org/10.1103/PhysRevB.78.184417)

PACS number(s): 75.30.Ds, 75.30.Et, 78.70.Nx

I. INTRODUCTION

Many important magnetic materials, such as colossal magnetoresistive manganites and high-temperature superconductors, are based on perovskite transition-metal oxides. The ground states and phases of these materials are known to depend sensitively on the energy scales of magnetic, orbital, vibrational, and electronic degrees of freedom.^{1,2} Various spectroscopic techniques are employed to determine these energy scales and the coupling between them, in an effort to understand and control the myriad of physical properties of these compounds.

The magnetic energy scale is set by the exchange energy between magnetic ions. It is purely quantum mechanical in origin and can arise from many different processes originating from the exchange of electrons between magnetic ions, such as direct exchange, superexchange, and double exchange. In insulating transition-metal oxide materials, the superexchange interaction depends on the overlap of metal *d* orbitals on neighboring sites via oxygen ligands. The rules for determining the sign [ferromagnetic (F) or antiferromagnetic (AF)] and strength of the superexchange between neighboring ions were established early on.³ A brief summary of these rules as applied to perovskites is as follows: two half-filled (or empty) orbitals in a (180°) bonding configuration have antiferromagnetic exchange, while a half filled and an empty orbital in a bonding configuration have ferromagnetic exchange.

In cubic perovskites, F exchange is not expected since all ionic sites are equivalent. Such is the case for LaFeO_3 , where each Fe^{3+} ion has a half-filled $3d^5$ configuration and all exchange interactions are AF, leading to a *G*-type magnetic structure (with all neighboring magnetic ions aligned antiparallel). However, metal ions with an orbital degeneracy are often relieved of this degeneracy by orbital ordering (due to Jahn-Teller distortions, for example). Orbital ordering can

make neighboring ions inequivalent and often leads to the presence of both F and AF interactions in the nominally cubic perovskites. This is true for LaMnO_3 , where a Jahn-Teller distortion elongates the oxygen octahedra and lifts the orbital degeneracy of the $\text{Mn}^{3+} t_{2g}^3 e_g^1$ ion. Staggering of the elongated axis in the *ab* plane minimizes strain and causes ordering of $e_g(3x^2-r^2/3y^2-r^2)$ orbitals. In the *ab* plane, e_g orbitals on all neighboring ions have a half-filled/empty configuration, leading to F exchange, while overlaps of the t_{2g} orbitals along the *c* axis remain AF (half filled/half filled). The net result is the *A*-type magnetic structure of ferromagnetic *ab* planes coupled antiferromagnetically to neighboring planes along *c*. In LaVO_3 , the degeneracy of the $\text{V}^{3+} t_{2g}^2$ ionic configuration is lifted by orbital ordering resulting in full occupancy of the *xy* orbital and staggered occupancy of the *xz/yz* orbital in all three cubic directions. This orbital ordering leads to the *C*-type magnetic structure of AF planes coupled ferromagnetically along *c*.

The energy of the exchange interactions in these and other perovskite magnets is most commonly determined by measurement of the spin-wave dispersions using inelastic neutron scattering (INS) on single-crystal samples. Such measurements can be time consuming (taking a week or more of measurement time) and depend on the availability of large single crystals. In this paper, we show that the different exchange interactions in the *ab* plane and along the *c* axis (termed the magnetic exchange anisotropy) in simple systems can be obtained rapidly by measurement of inelastic neutron scattering from powders. Inelastic neutron scattering from powder samples gives information on the spin-wave spectrum related to the spin-wave density of states (SWDOS). Such measurements can take as little as a few hours to complete and allow for efficient systematic studies of the dependence of exchange interactions on temperature and composition.

TABLE I. Experimental conditions and data analysis parameters for neutron-scattering measurements on LaMnO₃, LaVO₃, and LaFeO₃.

Compound	Magnetic ordering	E_i (meV)	Low-angle range	High-angle range
LaMnO ₃	A type	75	12°–42°	60°–120°
LaVO ₃	C type	75	7°–32°	60°–110°
LaFeO ₃	G type	160	1°–31°	55°–95°

We present powder inelastic neutron data for the aforementioned compounds; LaFeO₃, LaVO₃, and LaMnO₃, as representative of *G*-, *C*-, and *A*-type antiferromagnets, respectively (Table I). The data are compared to calculations of the spin-wave spectra and their neutron-scattering cross sections using a Heisenberg model. The results show that the magnetic exchange anisotropy of F and AF interactions can be determined in a straightforward manner from powder data.

II. SPIN WAVES IN CUBIC PEROVSKITES

Spin waves in the cubic perovskite insulators can be described by the Heisenberg Hamiltonian. In the case where cubic symmetry is broken by charge or orbital orderings, exchange interactions can become anisotropic. For the simplest kind of anisotropy, the exchange within the perovskite *ab* plane (J_{ab}) and that along the *c* axis (J_c) have different values and can even have different signs. The Heisenberg Hamiltonian becomes

$$H = -J_{ab} \sum_{\langle i,j \rangle \| a,b} \mathbf{S}_i \cdot \mathbf{S}_j - J_c \sum_{\langle i,j \rangle \| c} \mathbf{S}_i \cdot \mathbf{S}_j - g\mu_B H_a \sum_i \sigma_i S_i, \quad (1)$$

where \mathbf{S}_i is the spin vector on the *i*th site. The subscripts $\langle i,j \rangle \| a,b$ (*c*) indicate that sums are restricted to nearest-neighbor spins in the *ab* plane and along the *c* axis. Exchange energies are defined such that a positive *J* represents ferromagnetic exchange. Uniaxial single-ion anisotropy is represented by an anisotropy field H_a that acts on spin \mathbf{S}_i and points along the local spin direction (given by $\sigma_i = \pm 1$).

In the following, we identify four different magnetic structures, one of which is ferromagnetic and the other three are antiferromagnetic varieties. The structures are differentiated by the signs of J_{ab} and J_c .

$$\begin{aligned} F \text{ type: } & J_{ab} > 0, \quad J_c > 0, \\ G \text{ type: } & J_{ab} < 0, \quad J_c < 0, \\ C \text{ type: } & J_{ab} < 0, \quad J_c > 0, \\ A \text{ type: } & J_{ab} > 0, \quad J_c < 0. \end{aligned} \quad (2)$$

The spin-wave dispersions for each type of magnetic ordering are obtained from a linear expansion (spin-wave expansion) of the Heisenberg model.⁴ When the single-ion anisotropy is zero, the dispersions are

$$\hbar\omega_F(\mathbf{q}) = 2S\{2J_{ab}[1 - \gamma_+(\mathbf{q})] + J_c[1 - \gamma_z(\mathbf{q})]\},$$

$$\hbar\omega_G(\mathbf{q}) = 2S\{(2|J_{ab}| + |J_c|)^2 - [2|J_{ab}|\gamma_+(\mathbf{q}) + |J_c|\gamma_z(\mathbf{q})]^2\}^{1/2},$$

$$\hbar\omega_C(\mathbf{q}) = 2S\{[2|J_{ab}| + J_c[1 - \gamma_z(\mathbf{q})]]^2 - 4J_{ab}^2\gamma_+^2(\mathbf{q})\}^{1/2},$$

$$\hbar\omega_A(\mathbf{q}) = 2S\{[2J_{ab}[1 - \gamma_+(\mathbf{q})] + |J_c|]^2 - J_c^2\gamma_z^2(\mathbf{q})\}^{1/2}, \quad (3)$$

where $\gamma_+(\mathbf{q}) = \frac{1}{2}(\cos q_x a + \cos q_y a)$, $\gamma_z(\mathbf{q}) = \cos q_z a$, \mathbf{q} is the spin-wave momentum, and *a* is the cubic perovskite lattice constant. The dispersions for each magnetic structure are shown in Fig. 1 for the case where $|J_{ab}| = |J_c|$. The notation for labeling the zone-boundary reciprocal space positions are found in Kovalev.⁵ The spin-wave density of states (DOS) is the distribution of spin-wave energies and is determined by the summation over all wave vectors in the Brillouin zone (\mathbf{q}),

$$g(\omega) = \frac{1}{N} \sum_{\mathbf{q}} \delta[\omega - \omega(\mathbf{q})]. \quad (4)$$

The densities of states are also shown for the four magnetic structure types in Fig. 1. In addition, Fig. 1 indicates the energies of the various extremal features in the SWDOS [van Hove singularities (vHs)] for any J_{ab} and J_c .

III. SPIN-WAVE DENSITY OF STATES

If $|J_{ab}| = |J_c|$, it is clear that the four types of ordering are easily discernible from the spin-wave dispersions and densities of states. Figure 2 shows the SWDOS for each type of ordering in the case of $|J_{ab}| = |J_c|$. The maximum spin-wave energy increases as more ferromagnetic bonds are introduced. The *F*-, *A*-, *C*-, and *G*-type structures have the maximum spin-wave energies of $12J_{ab}S$, $10J_{ab}S$, $8J_{ab}S$, and $6J_{ab}S$, respectively.

In order to determine the exchange constants from powder samples, one must consider the degree of information available in the SWDOS. When $|J_{ab}| \neq |J_c|$, the positions of the vHs in the SWDOS allow identification of the exchange energies for each of the structure types:

F type: The SWDOS consists of five vHs as shown in Fig. 1(a). The vHs corresponding to zone-boundary spin waves along the *c* axis or in the *ab* plane lead directly to the corresponding exchange constants. Other zone-boundary spin waves give sums of the exchange constants. Figure 3(a) shows how the spectral features of the *F*-type magnet develop as the ratio $|J_c/J_{ab}|$ changes. In the limit that $J_c = 0$, the SWDOS of a two-dimensional (2D) ferromagnet consists of a sharp peak at $4|J_{ab}|S$ and an upper cutoff at $8|J_{ab}|S$.

A type: The SWDOS consists of several vHs as indicated in Fig. 1(b). The most useful for determining the exchange constants (in units of $|J_{ab}|S$) are the maximum spin-wave cutoff $[2(4 + |J_c/J_{ab}|)]$, the high energy edge of the central band $[2(2 + |J_c/J_{ab}|)]$ and the low-energy cusp $(2|J_c/J_{ab}|)$. Identification of any two of these vHs is sufficient to determine both $J_{ab}S$ and J_cS . For example, $J_{ab}S$ can be determined by the difference of the two highest energy vHs identified here (equal to $4|J_{ab}|S$). Figure 3(b) shows how the spectral

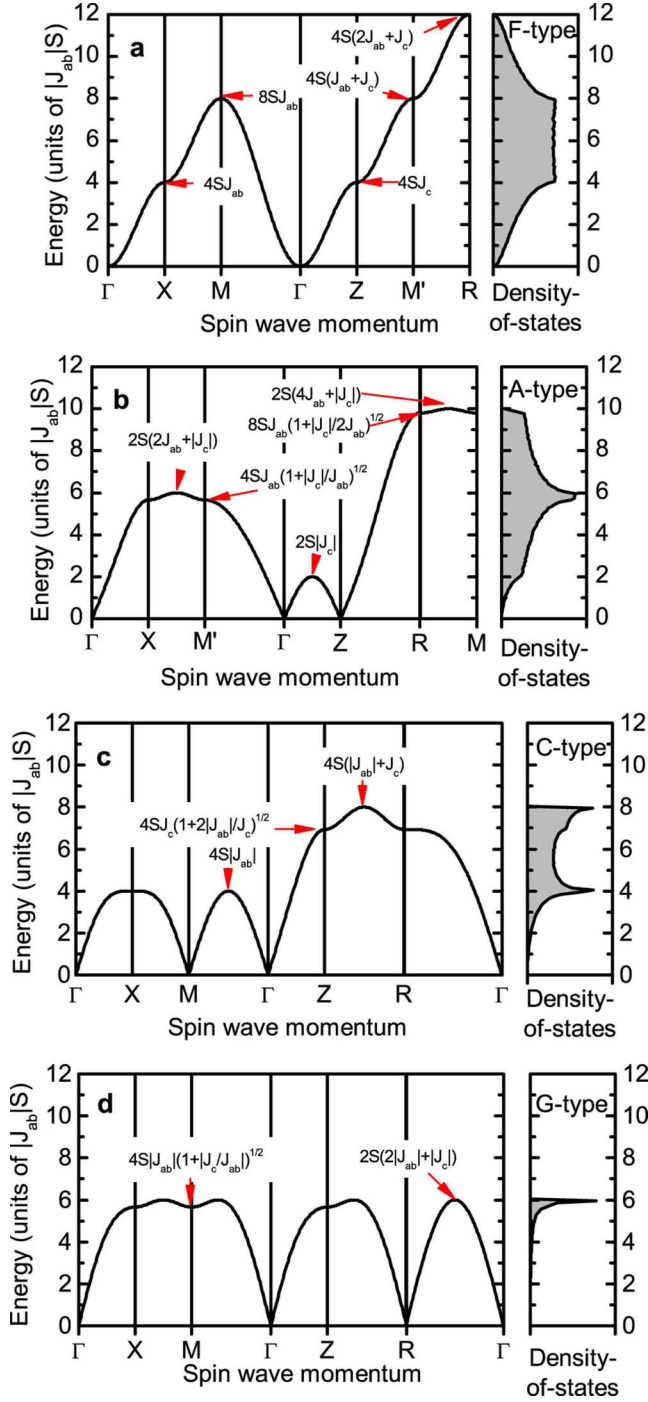


FIG. 1. (Color online) The spin-wave dispersion along various symmetry directions (left panels) and the spin-wave density of states (right panel) for (a) *F*-type, (b) *A*-type, (c) *C*-type, and (d) *G*-type perovskite magnets. Red arrows and labels indicate the energies of the extrema in the dispersion that give rise to van Hove singularities in the density of states.

features of the *A*-type antiferromagnet develop as the ratio $|J_c/J_{ab}|$ changes. As $|J_c|$ becomes relatively small (in the approach to a 2D ferromagnet), the central band collapses to a single energy at $4|J_{ab}|S$, the cusp just below the cutoff energy disappears, and the lowest-energy cusp at $2|J_c|S$ disappears.

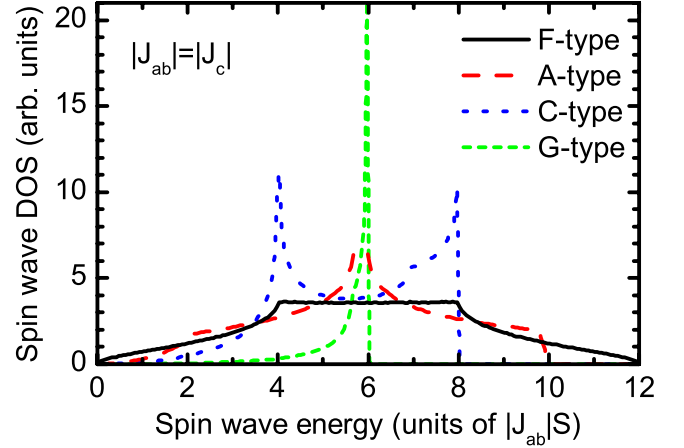


FIG. 2. (Color online) Spin-wave density of states for *F*-, *A*-, *C*-, and *G*-type magnets in the case where $|J_{ab}| = |J_c|$.

This is of course identical to the same limit in the *F*-type magnet discussed above.

C type: The SWDOS consists of three vHs, as shown in Fig. 1(c). The lowest-energy peak is due to zone-boundary spin waves in the basal plane and depends only on $|J_{ab}|S$, while the splitting of the two main peaks in the SWDOS gives J_cS directly. The development of the spectral features of the *C*-type antiferromagnet with the ratio $|J_c/J_{ab}|$ are shown in Fig. 3(c). As J_c becomes relatively small in the limit of the 2D antiferromagnet, the two main peaks merge into a single peak at $4|J_{ab}|S$.

G type: The SWDOS consists of a single sharp peak at the cut-off energy with a very weak cusplike vHs just below the cutoff energy. The energy of the peak in the density of states (DOS) is determined by the average exchange $\langle J \rangle = (4J_{ab} + 2J_c)/6$. As shown in Fig. 3(d), varying the ratio J_c/J_{ab}

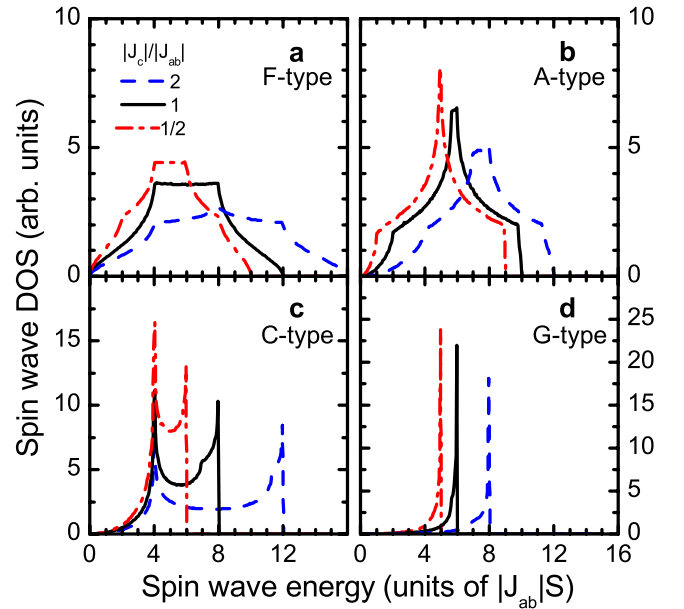


FIG. 3. (Color online) Spin-wave density of states for different ratios of the exchange $|J_c/J_{ab}|$ for (a) *F*-type, (b) *A*-type, (c) *C*-type, and (d) *G*-type magnets.

shifts the entire spectrum. The weak second vHs is often masked by the finite-energy resolution of the neutron spectrometer and in this case it is possible to determine only the average exchange $\langle J \rangle$.

IV. MEASUREMENTS

In order to test the predictions made in the Heisenberg model calculations above, inelastic neutron-scattering measurements were performed on the Pharos spectrometer at the Lujan Center of Los Alamos National Laboratory. Pharos is a direct geometry time-of-flight spectrometer and measures the scattered intensity over a wide range of energy transfers ($\hbar\omega$) and angles between 1° – 140° , allowing determination of a large swath of the scattered intensity, $S(Q, \omega)$, as a function of momentum transfer ($\hbar Q$) and $\hbar\omega$.

Powder samples of LaMnO_3 (LMO), LaVO_3 (LVO), and LaFeO_3 (LFO) were prepared by conventional solid-state reaction method and subsequently annealed to tune oxygen stoichiometry. Samples weighed approximately 50 g each and were characterized for phase purity by x-ray powder diffraction. Powders were packed in flat aluminum cans oriented at 45° or 135° to the incident neutron beam and INS spectra for LMO, LVO, and LFO, were measured with incident energies (E_i) of 75, 75, and 160 meV, respectively. The time-of-flight data were reduced into $\hbar\omega$ and scattering angle (2θ) histograms and corrections for detector efficiencies, empty can scattering, and instrumental background were performed.

Unpolarized inelastic neutron scattering contains contributions from both magnetic and phonon scatterings. In order to isolate the spin-wave spectrum, the magnetic scattering must be separated from the phonon scattering. This is accomplished by using the fact that the magnetic scattering falls off with Q (or 2θ) due to the magnetic form factor, while phonon scattering increases like Q^2 . Figure 4(a) shows the full spectrum for LFO at $T=10$ K as a function of 2θ and $\hbar\omega$, as reported previously.⁶ The band at 75 meV has intensity that falls off with 2θ , indicating that it is magnetic in origin. Data summed over the high-angle range contain mainly phonon scattering [Fig. 4(b)], while the low-angle range contains scattering from both phonons and spin waves [Fig. 4(c)]. The magnetic scattering component can be estimated by subtracting the high-angle data from low-angle data after scaling by a constant factor, as shown in Fig. 4(c) for LFO. Figure 4(d) shows that the resulting magnetic intensity estimated for LFO indeed consists of a single peak at $\hbar\omega \sim 75$ meV consistent with the G -type SWDOS shown in Fig. 3(d).

In the difference plot shown in Fig. 4(d), the strong peak at 0 meV is elastic scattering containing both nuclear and magnetic contributions that cannot be separated by the difference method. The very weak peaks at ~ 20 and 30 meV arise from imperfect phonon subtraction. The subtraction of the phonon intensity is subjected to error, primarily due to the fact that the scaling of phonon intensity from high angles to low angles is only expected to work for incoherent scattering from a monatomic sample. For real multicomponent samples, the phonon intensity may not scale uniformly to low Q due to coherent scattering effects (dependence of the

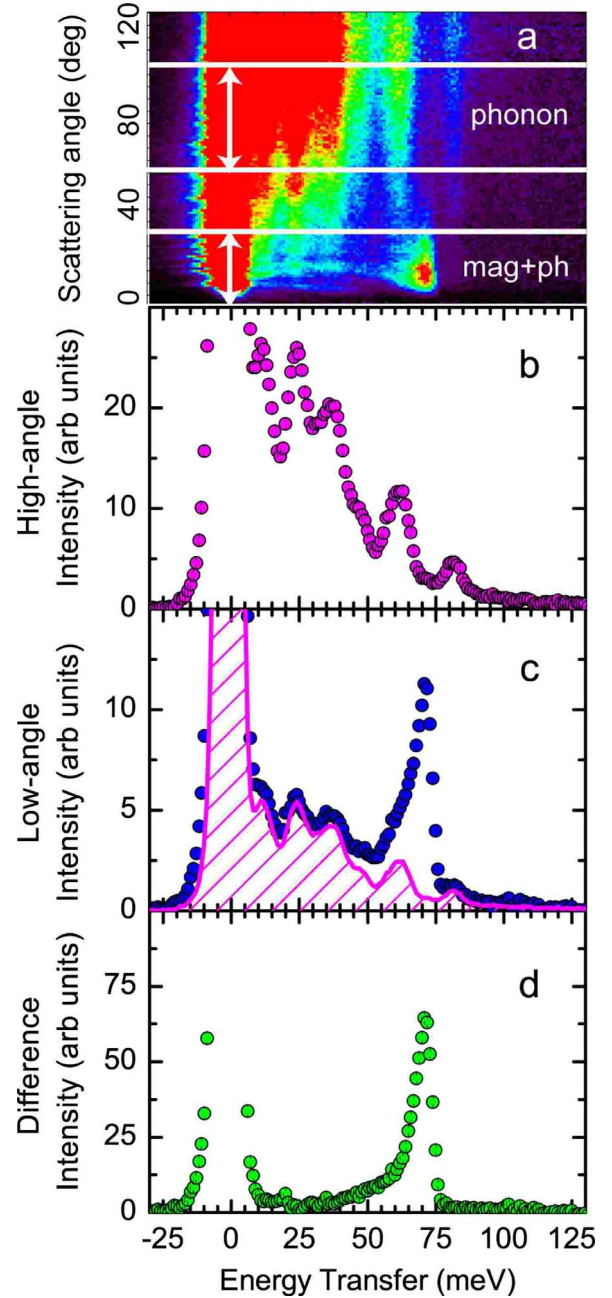


FIG. 4. (Color online) (a) Inelastic neutron-scattering intensity of LaFeO_3 (color scale) versus scattering angle and energy transfer at $T=10$ K and $E_i=160$ meV. Horizontal white lines delineate regions of predominantly phonon and magnetic scattering. (b) Neutron intensity summed over the high-angle range from 55° – 95° originating mainly from phonons. (c) Neutron intensity summed over the low-angle range from 1° – 30° (dots) and phonon background from scaled from high-angle sum (hatched region). (d) Intensity difference between low- and high-angle sums, giving mainly magnetic scattering from LFO at $T=10$ K.

phonon cross section on Q) and also due to the different Debye-Waller factors for each component. It is difficult to quantify this error without detailed phonon models, however, based on the general agreement between the isolated magnetic scattering and the calculations discussed below, the introduced errors are often small. Nonetheless, when we dis-

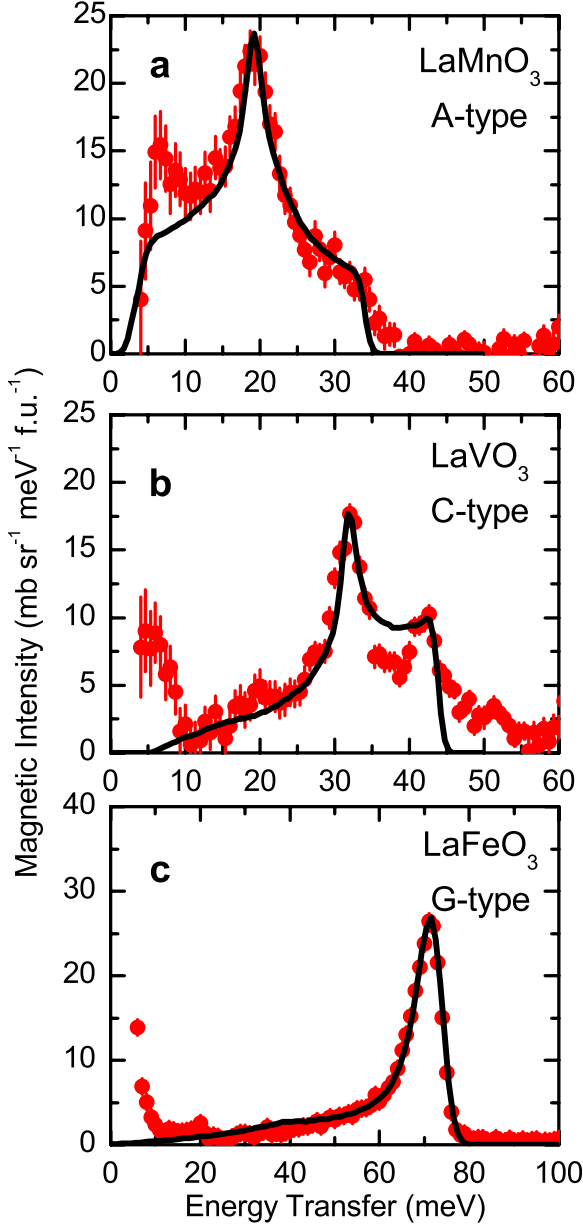


FIG. 5. (Color online) Extracted angle-averaged magnetic intensity (dots) versus energy compared to the intensity calculated from a Heisenberg model for the spin waves for (a) LaMnO_3 , (b) LaVO_3 , and (c) LaFeO_3 .

cuss the magnetic intensity throughout the remainder of the paper, it is subjected to these limitations.

The LMO and LVO data were treated in a similar fashion to the LFO data (details in Table I). Figure 5 shows the isolated magnetic intensity for the three different antiferromagnets. In each case, the magnetic spectra share similar features to the respective calculated SWDOS shown in Figs. 2 and 3.

V. CALCULATIONS OF THE SCATTERED INTENSITY

When performing an INS experiment on a powder, the resulting INS intensities arise from the averaging of the

inelastic-scattering structure factor $S(\mathbf{Q}, \omega)$ over all orientations of the crystallites. In favorable circumstances, it is even possible to study excitations from grain-aligned polycrystalline samples,⁷ where some orientational information is retained. Despite the orientational averaging, the spectra can show evidence of the spin-wave dispersions, especially at low angles (within the first Brillouin zone) and in the vicinity of the first few magnetic Bragg peaks. Such dispersive features are clearly seen in the intensity plots of $S(Q, \omega)$ in Figs. 6(a), 6(c), and 6(e) for LMO, LVO, and LFO, respectively. Due to the weighting of the spin-wave modes by coherent scattering intensities, the Q -averaged intensity, $S(\omega)$, as shown in Fig. 5 does not necessarily give the SWDOS. This is only true in the incoherent-scattering approximation, which does not apply to the case of scattering from a magnetically ordered system. Therefore, model calculations of the powder averaged spin-wave intensities are necessary for accurate comparison to the data.

Numerical calculations of the spin waves in the linear approximation to the Heisenberg model give not only the dispersion relation $\omega_n(\mathbf{q})$ for the n th (degenerate) branch [as shown in Eq. (4)] but also the spin-wave eigenvectors, $T_{ni}(\mathbf{q})$, for the i th spin in the magnetic unit cell. The dispersion and associated eigenvectors can be used to calculate the spin-wave structure factor for unpolarized neutron energy-loss scattering from a single-crystal sample, $S_{\text{mag}}(\mathbf{Q}, \omega)$.

$$S_{\text{mag}}(\mathbf{Q}, \omega) = \frac{1}{2}(\gamma r_o)^2 \left[1 + \frac{(\hat{\mu} \cdot \mathbf{Q})^2}{Q^2} \right] \times \sum_n \left| \sum_i F_i(\mathbf{Q}) \sigma_i \sqrt{S_i} T_{ni}(\mathbf{q}) e^{-i\mathbf{Q} \cdot \mathbf{d}_i} \right|^2 \times [n(\omega) + 1] \delta[\omega - \omega_n(\mathbf{q})], \quad (5)$$

where the i th spin with magnitude S_i pointed in direction $\hat{\mu}$ is located at position \mathbf{d}_i . $\sigma_i = \pm 1$ is the direction of the spin relative to the quantization axis $\hat{\mu}$ for a collinear spin structure. $\mathbf{q} = \mathbf{Q} - \boldsymbol{\tau}$ is the spin-wave wave vector in the first Brillouin zone. Finally, the function $n(\omega)$ is the temperature dependent Bose factor and $F_i(\mathbf{Q}) = \frac{1}{2} g_i f_i(\mathbf{Q}) e^{-W_i(\mathbf{Q})}$ is a product of the Lande g factor, magnetic form factor, and Debye-Waller factor for the i th spin, respectively. The constant $(\gamma r_o)^2 = 290.6$ millibarns allows calculations of the cross section to be reported in absolute units of millibarns Steradian⁻¹ meV⁻¹ and (formula unit)⁻¹. For the simple perovskite magnets studied here, all ions in the magnetic cell are considered to be equivalent. The structure factor can then be written as

$$S_{\text{mag}}(\mathbf{Q}, \omega) = \frac{1}{2}(\gamma r_o)^2 S F^2(\mathbf{Q}) \left[1 + \frac{(\hat{\mu} \cdot \mathbf{Q})^2}{Q^2} \right] \times \sum_n \left| \sum_i \sigma_i T_{ni}(\mathbf{q}) e^{-i\mathbf{Q} \cdot \mathbf{d}_i} \right|^2 \times [n(\omega) + 1] \delta[\omega - \omega_n(\mathbf{q})]. \quad (6)$$

In the calculations below, we use the isotropic magnetic form factors found in the international crystallography tables,⁸ and the Debye-Waller factor is set equal to one. The differential magnetic cross section that is measured in the inelastic

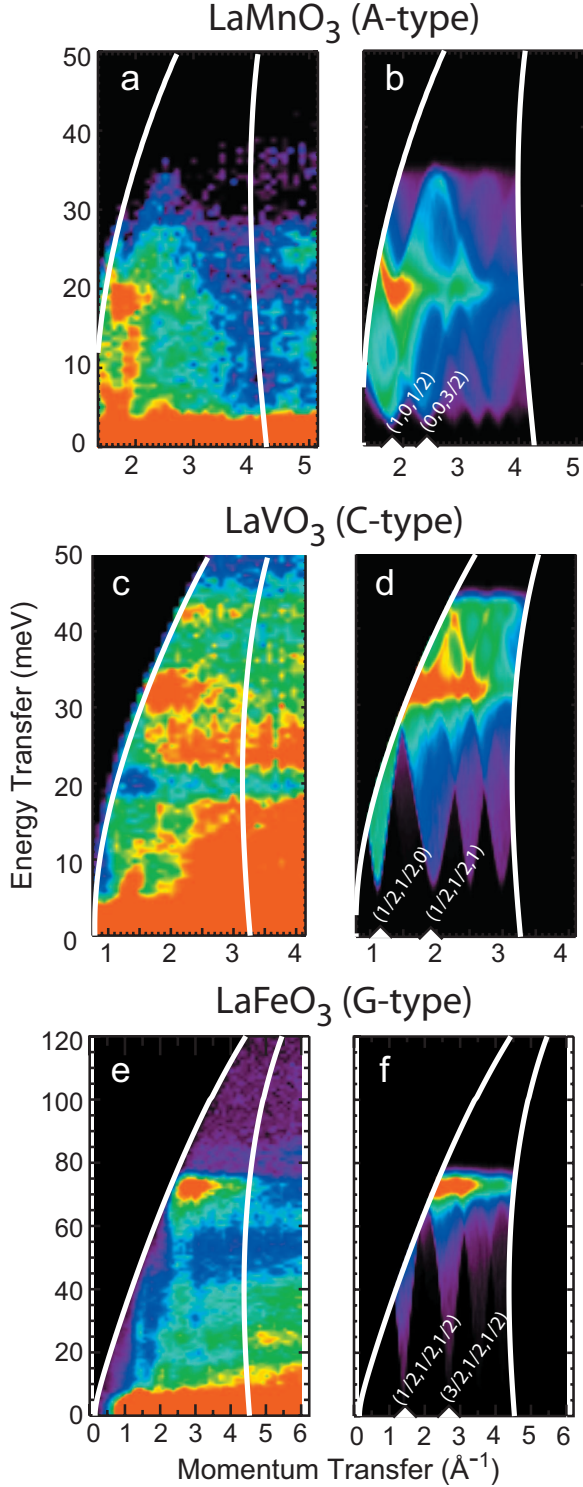


FIG. 6. (Color) Panels show the measured (left) and calculated (right) neutron intensities for [(a) and (b)] A-type LaMnO_3 , [(c) and (d)] C-type LaVO_3 , and [(e) and (f)] G-type LaFeO_3 . Experimental conditions and calculation parameters are given in the text. For the measured data in panels (a), (c), and (e), phonon intensities have not been subtracted and lead to a more complicated spectral image as discussed in the text. For each panel, the curved white lines indicate the low-angle summation regions leading to the corrected magnetic spectra in Fig. 5.

TABLE II. Values of the ionic spin, exchange energies, and uniaxial anisotropy energies used in calculations of the neutron-scattering intensity from spin waves.

Compound	S	J_{ab} (meV)	J_c (meV)	$g\mu_B H_a$ (meV)
LaMnO_3	2	1.85	-1.1	0.6
LaVO_3	1	-7.8	2.9	0.6
LaFeO_3	5/2	-4.87	-4.87	0

neutron-scattering experiments is proportional to the structure factor.

To compare Heisenberg model spin-wave results to the powder INS data, powder averaging of $S_{\text{mag}}(\mathbf{Q}, \omega)$ is performed by Monte Carlo integration over a large number of \mathbf{Q} vectors lying on a constant- Q sphere, giving the orientationally averaged $S_{\text{mag}}(Q, \omega)$ which depends only on the magnitude of Q . Figures 6(b), 6(d), and 6(f) show calculations of $S_{\text{mag}}(Q, \omega)$ (broadened by instrumental resolution) at 10 K for LMO, LVO, and LFO, respectively, and can be compared to the corresponding data in Figs. 6(a), 6(c), and 6(e). In order to properly calculate the structure factor, we use the structural parameters for the three compounds (which are orthorhombically distorted perovskite structures). In the case of LFO (Ref. 9) and also C-type YVO_3 ,¹⁰ the orthorhombic distortion leads to additional magnetic anisotropies that result in a weakly noncollinear structure due to the small canting of the magnetic moments. For the calculations presented here, we consider only the pure collinear structures with cubic exchange interactions J_{ab} and J_c . The values for J_{ab} , J_c , and H_a used in the calculations for each compound are shown in Table II. In the case of LMO, the anisotropy field was determined by Hirota *et al.*¹¹ from single-crystal dispersion measurements, and the exchange constants can be compared to the values obtained in that paper. For LVO, the anisotropy field was determined from cold neutron measurements of the anisotropy gap in powder samples.¹² The small anisotropy energies reported here have very little effect on the energy of the zone-boundary spin waves, which are determined primarily by the exchange.

The calculations can be summed over scattering angles in order to compare the equivalent angle-summed data, as shown in Fig. 5. Overall, the agreement between the data and calculations is excellent. This is a testament to the effectiveness of the Heisenberg model for these compounds in predicting not only the spin-wave energies but also the intensities. However, some differences observed in the comparison of data and calculation are worth noting. At low energies near to the elastic line, additional intensity is observed, most notably in the 5–10 meV range in $E_i=75$ meV data. The origin of this intensity is unclear, but it is possible that it originates from multiple elastic scattering. For LaMnO_3 , this additional scattered intensity, combined with insufficient elastic energy resolution, does not allow the observation of the low-energy vHs expected at ~ 6 meV that can be used to determine J_c . Higher-resolution measurements are required to obtain J_c exclusively.

The poorest agreement between data and calculation occurs for LaVO_3 in Fig. 5(b). While the data shows clear vHs

at ~ 32 and ~ 44 meV, the calculated intensity shows a shoulder rather than a clear peak in the upper vHs, indicating that the Heisenberg model does not reproduce the LVO spin-wave intensities with the same accuracy as for LMO and LFO. Much of this discrepancy may be due to the physics of LVO, where C -type magnetic structure can arise from either weak Jahn-Teller driven orbital ordering or orbital singlet formation. Competition between these two scenarios require spin-orbital coupling terms that go beyond the Heisenberg Hamiltonian.^{13,10} Also, additional intensity at 20 and 50 meV in LVO is likely due to improper phonon subtraction. This subtraction is made more difficult due to the small spin ($S = 1$) of the V ion, which leads to weaker spin-wave scattering [see Eq. (6)].

Figure 6 shows a comparison of the measured and calculated scattered intensities as a function of Q and $\hbar\omega$ for the three compounds. The calculation results in Figs. 6(b), 6(d), and 6(f) show clearly the coherent scattering of the powder averaged spin waves. The most obvious coherent scattering feature is the necking down of acoustic spin waves in the vicinity of allowed magnetic Bragg reflections. The characteristic ordering wave vectors for the different antiferromagnets are (0,0,1/2) for A type, (1/2,1/2,0) for C type, and (1/2,1/2,1/2) for G type (using the cubic indexing). The first two observed magnetic Bragg peaks in each case are indicated in Fig. 6. Additional coherent scattering features can also be seen for zone-boundary spin waves, where intensities tend to peak in between the allowed magnetic Bragg peaks. Figure 6 enforces the general agreement of the Heisenberg model calculations of the spin-wave intensity with neutron-scattering measurements. Unfortunately, the comparison of the Heisenberg model spin-wave intensities to the data is complicated because measurements also contain coherent phonon-scattering intensity. The phonon intensity bands present themselves mainly as horizontal (constant energy) streaks. A prominent phonon band can be seen, for example, at 25 meV in LVO [Fig. 6(c)], and at 25, 40, and 60 meV in LFO [Fig. 6(e)].

The success of the Heisenberg model in estimating the measured spin-wave intensities is better observed by plotting constant energy Q cuts, as shown in Fig. 7 for LMO. The plots show Q oscillations of the experimental magnetic spin-wave scattering above a background due mainly to phonon scattering and background/multiple scattering. A constant background and incoherent phonon-scattering intensity (proportional to Q^2) are added to the calculated spin-wave scattering in order to compare to the measured data. The agreement is excellent. The overall consensus is that the spin-wave intensities are well represented by the Heisenberg model, and it is promising that one can obtain more from powder data than just an estimate of the spin-wave DOS. Analysis of the full structure factor $S_{\text{mag}}(Q, \omega)$ may allow exchange interactions to be determined in more complicated magnetic structures or with interactions beyond nearest neighbor. However, a full analysis of powder averaged spin

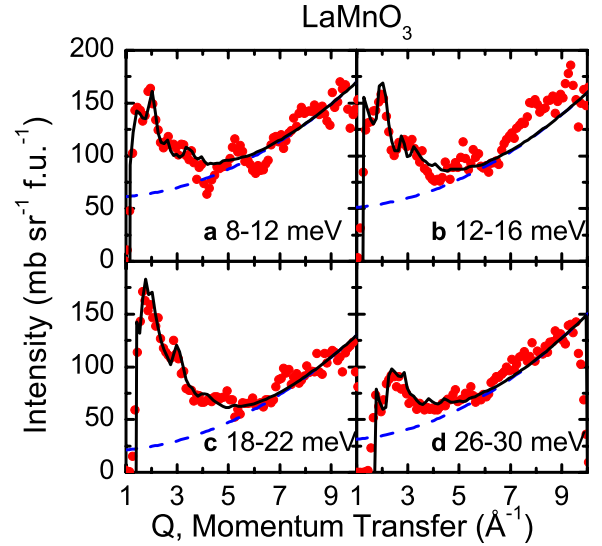


FIG. 7. (Color online) The Q dependence of the neutron-scattering data for different energy-transfer ranges in LaMnO_3 : (a) 8–12 meV, (b) 12–16 meV, (c) 18–22 meV, and (d) 26–30 meV. The red dots are the experimental data. The dashed lines are estimates of the incoherent phonon background plus multiple scattering. Solid lines are calculations of the polycrystalline averaged spin-wave scattering using the parameters in the text plus background.

waves requires better understanding of the phonon spectra and multiple scattering. In the future, we plan on combining fully coherent calculations of both phonons and spin waves to attempt a more ambitious analysis of the full $S(Q, \omega) = S_{\text{mag}}(Q, \omega) + S_{\text{phonon}}(Q, \omega)$.¹⁴

VI. SUMMARY

We have demonstrated that inelastic neutron-scattering experiments on powders, in combination with calculations of the spin-wave scattering in a Heisenberg model, can give detailed information about the exchange interactions in simple magnets. The agreement of not only the spin-wave DOS but also the Q dependence of coherent features in the spin-wave scattering gives hope that even more complicated magnetic systems can be analyzed using the full $S(Q, \omega)$. The advent of new spallation neutron sources, such as the Spallation Neutron Source, will allow the rapid measurements of samples with good statistics and make detailed systematic studies of magnetism possible.

ACKNOWLEDGMENTS

R.J.M. would like to thank F. Trouw, A. Llobet, and M. Hehlen for assistance with Pharos. Ames Laboratory is supported by the U.S. Department of Energy Office of Science under Contract No. DE-AC02-07CH11358. The work has benefited from the use of the Los Alamos Neutron Science Center at Los Alamos National Laboratory. LANSCE is funded by the U.S. Department of Energy under Contract No. W-7405-ENG-36.

*Present address: National Institute of Standards and Technology, Center for Neutron Research, Gaithersburg, Maryland 20899.

¹Y. Tokura and N. Nagaosa, *Science* **288**, 462 (2000).

²Y. Tokura, *Rep. Prog. Phys.* **69**, 797 (2006).

³J. Goodenough, *Magnetism and the Chemical Bond* (Wiley, New York, 1963).

⁴M. Raczkowski and A. M. Oles, *Phys. Rev. B* **66**, 094431 (2002).

⁵*Representations of the Crystallographic Space Groups*, edited by O. V. Kovalev (Gordon and Breach, Langhorne, PA, 1993).

⁶R. J. McQueeney, J. Ma, S. Chang, J. Q. Yan, M. Hehlen, and F. Trouw, *Phys. Rev. Lett.* **98**, 126402 (2007).

⁷U. Staub, F. Fauth, M. Guillaume, J. Mesot, A. Furrer, P. Dosanjh, and H. Zhou, *Europhys. Lett.* **21**, 845 (1993).

⁸P. J. Brown, in *International Tables for Crystallography*, edited by E. Prince (Kluwer, Dordrecht, 2004), pp. 454–461.

⁹T. Peterlin-Neumaier and E. Steichele, *J. Magn. Magn. Mater.* **59**, 351 (1986).

¹⁰C. Ulrich, G. Khaliullin, J. Sirker, M. Reehuis, M. Ohl, S. Miyasaka, Y. Tokura, and B. Keimer, *Phys. Rev. Lett.* **91**, 257202 (2003).

¹¹K. Hirota, N. Kaneko, A. Nishizawa, and Y. Endoh, *J. Phys. Soc. Jpn.* **65**, 3736 (1996).

¹²J.-Q. Yan (unpublished).

¹³G. Khaliullin, P. Horsch, and A. M. Oles, *Phys. Rev. Lett.* **86**, 3879 (2001).

¹⁴R. J. McQueeney (unpublished).